UC Berkeley
UC Berkeley Previously Published Works

Title
The birth and evolution of solvated electrons in the water

Permalink
https://escholarship.org/uc/item/94m2f63g

Journal
Proceedings of the National Academy of Sciences of the United States of America, 120(8)

ISSN
0027-8424

Authors
Novelli, Fabio
Chen, Kaixuan
Buchmann, Adrian
et al.

Publication Date
2023-02-21

DOI
10.1073/pnas.2216480120

Peer reviewed

🔓 OPEN ACCESS

The birth and evolution of solvated electrons in the water

Fabio Novelli[a,1] 🆔, Kaixuan Chen[b,c], Adrian Buchmann[a] 🆔, Thorsten Ockelmann[a], Claudius Hoberg[a] 🆔, Teresa Head-Gordon[b,c,d,e,f,1] 🆔, and Martina Havenith[a,1] 🆔

The photo-induced radiolysis of water is an elementary reaction in biology and chemistry, forming solvated electrons, OH radicals, and hydronium cations on fast time scales. Here, we use an optical-pump terahertz-probe spectroscopy setup to trigger the photoionization of water molecules with optical laser pulses at ~400 nm and then time-resolve the transient solvent response with broadband terahertz (THz) fields with a ~90 fs time resolution. We observe three distinct spectral responses. The first is a positive broadband mode that can be attributed to an initial diffuse, delocalized electron with a radius of (22 ± 1) Å, which is short lived (<200 fs) because the absorption is blue-shifting outside of the THz range. The second emerging spectroscopic signature with a lifetime of about 150 ps is attributed to an intermolecular mode associated with a mass rearrangement of solvent molecules due to charge separation of radicals and hydronium cations. After 0.2 ps, we observe a long-lasting THz signature with depleted intensity at 110 cm^{-1} that is well reproduced by ab initio molecular dynamics. We interpret this negative band at 110 cm^{-1} as the solvent cage characterized by a weakening of the hydrogen bond network in the first and second hydration shells of the cavity occupied by the localized electron.

solvated electron | THz spectroscopy | ab initio MD

The solvated electron is a fundamental reaction intermediate in a variety of physical, chemical, and biological processes (1). For example, it has important roles in the energy transfer during photochemical and electrochemical phenomena (2), atmospheric chemistry (3), radiation damage of biological matter (4), and medical therapeutics (5). When the intensity of the visible electromagnetic radiation is high enough, photoionization of water molecules can occur in the liquid phase. As has been confirmed in many experimental and theoretical studies, the fully relaxed, solvated, or hydrated aqueous electrons are generated in less than 1 ps (6–13). In previous papers, it was proposed that the electronic charge density is localized in a cavity with a radius of ~2.5 Å (14–16) and surrounded by ~4 water molecules (17, 18), two of which are hydrogen bonded to the electron and the other two participating in the water–water network. This has been challenged (19–22) by the possibility that the electron might be more delocalized across waters rather than localized in a cavity.

In a seminal work (11), the Hamm and Jungwirth groups studied the kinetics of electrons generated in water by photoionization by recording the change in the maximum amplitude of the THz probe signal. Depending on the optical frequency (23, 24), pulse duration (25), and the amount of photons that are absorbed, the number and radius of the precursor of the delocalized solvated electron (26, 27) can vary. Previously, the transient increase in THz absorption over the frequency range of 1–2 THz was described by a particle in the box picture, which postulates an increase in the frequency of the absorption mode upon localization of the solvated electron (11). In line with this model, the overwhelming partial absorption feature of the electron with the water molecules in the first and second shells will shift outside of the covered frequency range within less than 200 fs. The partial contribution originating from the negative cross-correlation between first and second hydration shells of the localized solvated electron—which is weaker in intensity—should be present for the entire time, up to the largest pump–probe delay of 250 ps. However, this cross-correlation part was not resolved in their experiments.

Here, we use an optical-pump terahertz-probe (OPTP) spectroscopy setup that, unlike previous work, allows to record the frequency-resolved change in the THz spectrum as a function of the pump–probe delay, t_{PP}, and to follow the time evolution of the solvated electron. From the creation of the delocalized solvated electron, subsequent charge separation of the hydronium and the generated OH radicals, and finally electron localization, we measure frequency-resolved changes in the THz spectrum, which probes the intermolecular modes of the hydrogen-bonded water molecules between about 30 cm^{-1} and 200 cm^{-1} with up to a pump–probe delay of 250 ps and with a time resolution of ~90 fs. Upon photoexcitation at 9.3 eV, we observe a short lived (< 200 fs) transient THz absorption at

Significance

The solvated electron is a fundamental reaction intermediate in physical, chemical, and biological processes. Here, we follow the birth and time evolution of the solvated electron with state-of-the-art, solvent-sensitive kinetic terahertz spectroscopy and molecular simulations. We observe a spectroscopic signature attributed to the delocalized electron, followed by the onset of a solvent perturbation caused by the initial charge separation of hydroxyl radicals and hydronium cations. Due to the high experimental sensitivity, we observe in addition the spectroscopic signature of the localized electron, which is long lasting (>250 ps): This reveals a weakening of the hydrogen bond network of the cage, which correlates with an increase in entropy due to greater orientational motions of the surrounding hydration layers.

(169 ± 13) cm^{-1}, which corresponds to a diffuse, highly excited and delocalized Rydberg state (23–26, 28–30), e.g., an exciton (26, 31) spreading over multiple hydrogen-bonded water molecules with a radius of (22 ± 1) Å. We also observe a previously unknown absorption feature with a lifetime of ~150 ps at 60 − 100 cm^{-1}, which we assign to a translational mode of the solvent triggered by the separation of the molecular complex containing the photo-generated positive charge, OH(H$_3$O$^+$). We propose that the excitation of this translational mode explains the experimentally observed nonthermal structural bond distance distribution as observed by time-resolved electron diffraction of OH-H$_3$O$^+$ pair decay subsequent to photoexcitation of bulk water, as recently reported by Lin et al. (32). With the aid of dedicated ab initio molecular dynamic (AIMD) simulations, this state-of-the-art optical setup revealed the transient signature of the solvent cavity formation of the localized electron, which is imprinted into the perturbed, dynamic terahertz spectrum of the collective water modes at ~110 cm^{-1}. Based on AIMD simulations, we are able to reveal the molecular details of the weakening of the underlying collective translational and intermolecular stretching motions of the hydrogen bond network (33–38), which leads to the experimentally observed decrease in absorption compared with bulk water.

Results

THz spectroscopy probes the intermolecular modes of bulk water and is very sensitive to any changes of the radial or angular part of the water–water potential. The most characteristic modes are the intermolecular stretch with a peak frequency at 200 cm^{-1} (7 THz) and the hindered rotations of water molecules in the

hydrogen bond network with a maximum in absorption around 700 cm^{-1} (20 THz). In a previous AIMD simulation study, upon introducing spatially resolved analyses, the sensitivity of THz spectroscopy is traced back to characteristic distance-dependent modulations of absorption intensities for bulk water. The prominent peak at ~200 cm^{-1} is found to be dominated by first-shell dynamics, whereas a concerted motion involving the second solvation shell contributes most significantly to the absorption at about 80 cm^{-1} ≈ 2.4 THz (34). Cross-correlating these modes with the local dipole demonstrates that the integrated contribution to the total infrared activity for the mode around 2.4 THz is indeed very weak, which is consistent with the lack of any clear resonance around 80 cm^{-1} in the THz absorption spectrum, while the peak is present in Optical Kerr as well as Raman spectra.

Furthermore, for solvated cations and anions characteristic THz fingerprints, i.e., characteristic absorption features whose intensities scale linearly with electrolyte concentration, have been identified and assigned to so-called "rattling" modes of the charge in the hydrogen bond network (39, 40).

Here, we record OPTP spectra to probe the THz changes in the hydrogen bond network of the water upon the birth and the evolution of the solvated electron as a function of pump probe delay subsequent to photoionization of bulk water. The experimental setup is described in detail in ref. 41. As a probe, we used a broadband terahertz time-domain spectrometer in the frequency range between $\omega_{EOS} \sim 60$ cm^{-1} (1.8 THz) and ~240 cm^{-1} (7.2 THz). The source spectrum is shown in *SI Appendix*, Fig. S1. In Fig. 1*A*, we plot the frequency-dependent changes of the optical density (OD) of water in the probed THz range, after the optical excitation. We observe an instantaneous response, $\Delta OD(\omega_{EOS}, t_{PP})$,
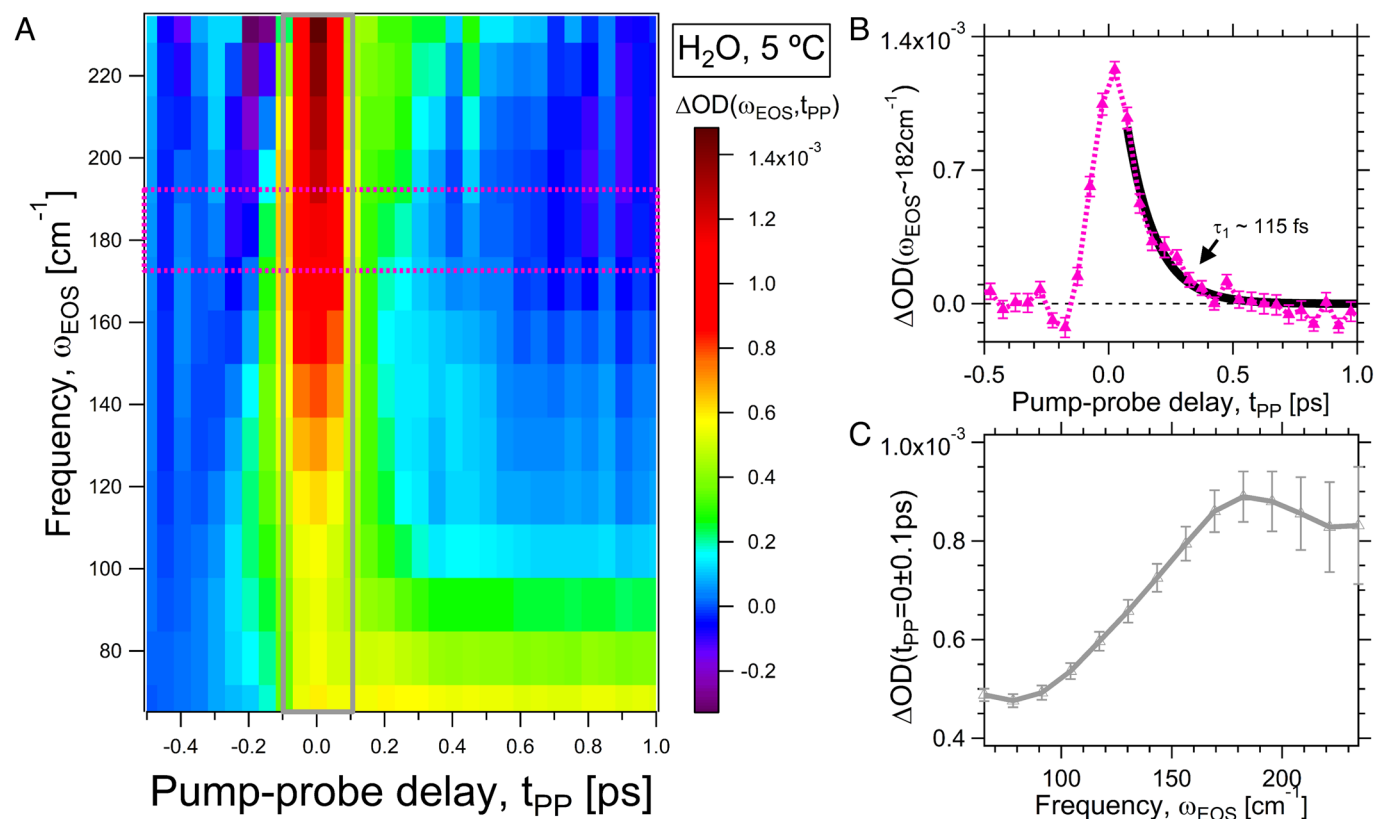

Fig. 1. Results of OPTP experiments on bulk water at 5 °C. (*A*) Transient change of the optical density, $\Delta OD(\omega_{EOS}, t_{PP})$, as a function of the probed THz frequency (ω_{EOS}) and the pump–probe delay (t_{PP}). The color scale on the right indicates a maximum signal of ~1.4 mOD. (*B*) Time-dependent change of the THz signal at $\omega_{EOS} \approx 180$ cm^{-1}, plotted versus pump–probe delay. The dashed purple trace is obtained by averaging the signal between the THz probe frequency $\omega_{EOS} = 169$ cm^{-1} and $\omega_{EOS} = 195$ cm^{-1}, as indicated by the purple box in *A*. (*C*) THz transient spectrum close to pump–probe overlap, $t_{PP} = (0 \pm 0.1)$ ps, plotted versus probed THz frequency (ω_{EOS}). The gray trace corresponds to an average of ΔOD between $t_{PP} = -0.1$ ps and $t_{PP} = +0.1$ ps.

which covers the entire frequency range from 60 to 240 cm^{-1} at pump–probe overlap ($t_{pp} = 0$). In Fig. 1 B and C, we plot the transient signal and the spectrum of the transient OD at short pump–probe delays. The detected transient THz spectrum is broad and centered at $\omega_{EOS} \sim 180$ cm^{-1} for $t_{pp} = (0 \pm 0.1)$ ps as seen in the gray curve in Fig. 1C. The time-dependent signal at $\omega_{EOS} = (182 \pm 13)$ cm^{-1} (purple curve in Fig. 1B) can be described by a single exponential function with a time constant $\tau_1 \sim 115$ fs. The fit results are summarized in *SI Appendix*, Table ST1. For confirmation, we checked that similar time constants are obtained when the raw transient THz data are fitted; see *SI Appendix*, Fig. S2.

The amount of absorbed photons can be quantified by measurements as a function of the pump intensity, I. As detailed in *SI Appendix*, Fig. S4, we found that the signal at $\omega_{EOS} = (182 \pm 13)$ cm^{-1} and $t_{pp} = (0 \pm 0.1)$ ps follows a quadratic behavior below $I \sim 0.8$ TW/cm^2 and saturates at higher pump intensities. In contrast, the transient response at $\omega_{EOS} = (78 \pm 13)$ cm^{-1} and $t_{pp} = (20 \pm 10)$ ps follows a cubic dependence below $I \sim 0.8$ TW/cm^2 and is consistent with previous publications (8, 11, 13, 24, 27, 42, 43); see also *SI Appendix*, Fig. S5. The predicted reflection losses at the air–water interfaces agree well with the results of the experiment, implying that the amount of optical pump energy absorbed by the liquid water jet must be less than the error bars, about 0.5%. From this, we estimate the maximum temperature increase in the liquid water sample to $+0.2$ °C (*Methods* and *SI Appendix*). Based on a comparison with the expected changes of ΔOD and Δn for bulk water with an increase in temperature of $+0.2$ °C (44–46), we conclude that thermal effects can be neglected. In addition, in order to exclude that the presence of counter ions affects the measurements, we measured the change of the static, equilibrium optical density upon addition of 3.5 mM NaI in water (*SI Appendix*, Fig. S6D)

and compare it to the observed change in ΔOD measured upon photoexcitation.

Transient Signature of the Instantaneously Generated Electron. In order to decrease or increase the number of solvated electrons, we dissolved either 1 M nitrate anions (27, 47–50) or 50 mM iodide anions (51–56), respectively. The experimental results are shown in Fig. 2 A and B. As is known, the number of photo-generated electrons decreases by more than 70% by dissolving 1 M NaNO$_3$ in pure water (27, 47, 50). As shown in Fig. 2A, the dominant positive signal at pump–probe overlap, $t_{pp} = (0 \pm 0.1)$ ps, decreases by $\sim 40\%$ upon addition of the electron scavenger (NO$_3^-$). In contrast, we observe a 10-fold increase upon addition of 50 mM NaI, i.e., under experimental conditions where more precursors of the solvated electrons should be generated, in line with our expectations; see Fig. 2B and the *Methods* section for details. While the amplitudes of the signals at pump–probe overlap differ by one order of magnitude upon the dissolution of NaNO$_3$ and NaI, the spectral shape, reported in *SI Appendix*, Fig. S7, is similar, indicating the same underlying molecular processes.

We first want to focus on the initial signature of the photo-generated delocalized electron by comparing the results on bulk water and on an aqueous solution containing the electron scavenger, which is known to capture the pump-excited electron within less than 80 fs (27, 47, 48). Thus, the difference between the measurements performed on pure water (with excess electrons) and on an 1 M NaNO$_3$ aqueous solution (in which the majority of photo-generated electrons have been scavenged by the nitrate ion) is expected to reveal the THz spectral signature of the photo-generated electrons. The difference between the measurements on pure water and a 1 M NaNO$_3$ solution at short pump–probe delays is shown in Fig. 2C. It reveals a positive ($\Delta\Delta OD \approx 4 \cdot 10^{-4}$), high-frequency ($\omega_{EOS} \approx 170$ cm^{-1}), and short-lived response at
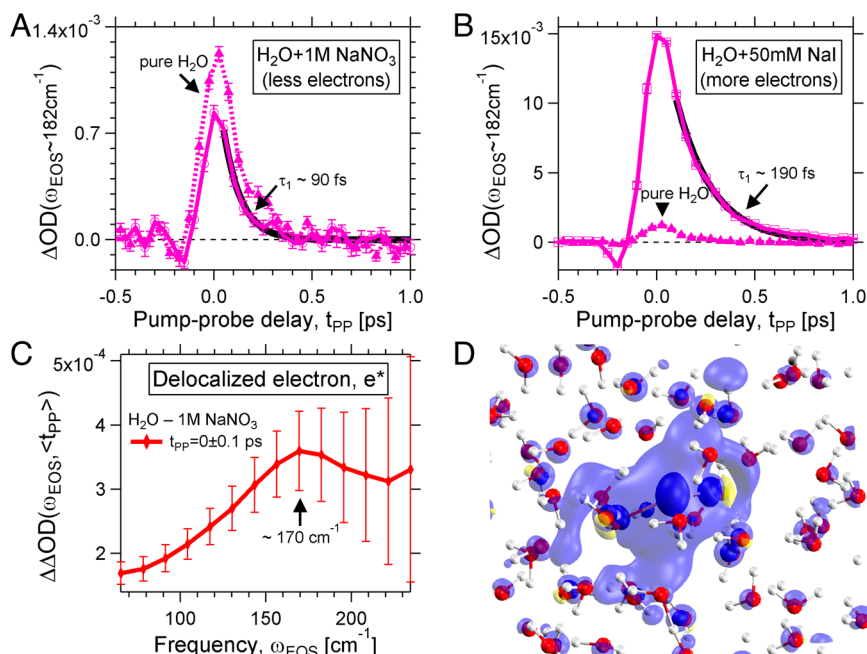

Fig. 2. Delocalized electron precursor generated by multiphoton excitation at 400 nm. (A) Time-dependent terahertz signal at the probe frequency $\omega_{EOS} = (182 \pm 13)$ cm^{-1} when the number of photo-generated electrons is reduced by a scavenger (1 M NaNO$_3$, solid purple curve, circles data points). The results on pure water are duplicated from Fig. 1B and shown with the dashed purple curve, solid triangles, for comparison. (B) Time-dependent terahertz signal at the probe frequency $\omega_{EOS} \sim 182$ cm^{-1} when the number of photo-generated electrons is increased by dissolution of iodide anions (50 mM NaI, purple squares). (C) We plot the difference between the transient optical densities, $\Delta\Delta OD$, measured in pure water and on a 1 M NaNO$_3$ aqueous solution at 5 °C, at the pump–probe delay $t_{pp} = (0 \pm 0.1)$ ps, as a function of THz probe frequency, ω_{EOS}. The transient signal is centered at (169 ± 13) cm^{-1}, where 13 cm^{-1} is the experimental frequency resolution. (D) Cartoon of the delocalized photo-generated electron shortly after pump-excitation.

$t_{PP} = (0 \pm 0.1)$ ps. The full map is shown in *SI Appendix*, Fig. S8. This overwhelming positive absorption is attributed to the autocorrelation of the charge with the first and second shell water. As shown in Fig. 2*C*, the initial signature of the pump-generated electron yields a broad peak with a center frequency of (169 ± 13) cm^{-1}. When we follow the model developed by the Jungwirth and Hamm groups (11), the first excitation energy of a particle in a box can be described as follows (14–16): $E = A/R_g^2$ with E excitation energy, A constant (equal to 84,688 cm^{-1} in ref. 11), and R_g radius of gyration. Thus, a transition at $E = (169 \pm 13)$ cm^{-1} corresponds to a radius of gyration equal to $R_g \approx (22 \pm 1)$ Å. This values is in excellent agreement with the average radius estimated before, independently, from the geminate recombination kinetics (27), ~22 Å. Thus, we propose that the mechanism of photoionization of liquid water at 400 nm is dominated by the molecular excitation of diffuse molecular states (57–59), akin to Rydberg states (23, 24, 26, 28–30) in a gas or Wannier excitons (26, 31) in a solid, rather than by autoionization (23, 25). A depiction of the initially delocalized photo-generated electron is shown in Fig. 2*D* from AIMD simulations (described further below) in which the electron is delocalized across several water molecules.

Excitation of a Low-Frequency Intermolecular Solvent Mode Initiated by Charge Separation. Fig. 3*A* shows the results on pure water up to a pump–probe delay of 250 ps. Next to the initial and fast-decaying feature, we clearly observe an additional, long-lived spectral feature characterized by an increase in amplitude at low frequencies ($\sim 60 - 100$ cm^{-1}). This feature rises with a time constant τ_2 within ~130 fs and ~200 fs and decays with a time constant τ_3 between 115 and 176 ps (*SI Appendix*, Table ST1). We display the spectrum of this long-lasting feature in gray in Fig. 3*B*. This transient THz spectrum resembles a remarkable Raman response of liquid water at equilibrium (60), which is shown with the black curve in Fig. 3*B*. The amplitude of this feature does not correlate with the number of photo-generated electrons; see Fig. 3*C*. Furthermore, the decay time is on the order of ~150 ps, which is shorter than the expected decay time of the relaxed, solvated aqueous electrons that was reported to be >300 ps in refs. 8, 11, 12, 23, 24, 42, 43, 61. Thus, we exclude the assignment of this feature to any spectral response directly associated with the solvated electron.

The emergence of this spectral feature is described by the time scale τ_2, which varies between ~130 fs and ~200 fs as detailed in *SI Appendix*, Table ST1. Previously, time scales between ~50 fs and ~250 fs were assigned to the formation of a "relaxed proton" in water (32, 62–68). Loh et al. (62) performed pulsed X-ray experiments and found two short time scales in the photoionization of liquid water: ~50 fs and ~180 fs, which were assigned to the decay of the photo-ionized cation H_2O^+ and to the relaxation
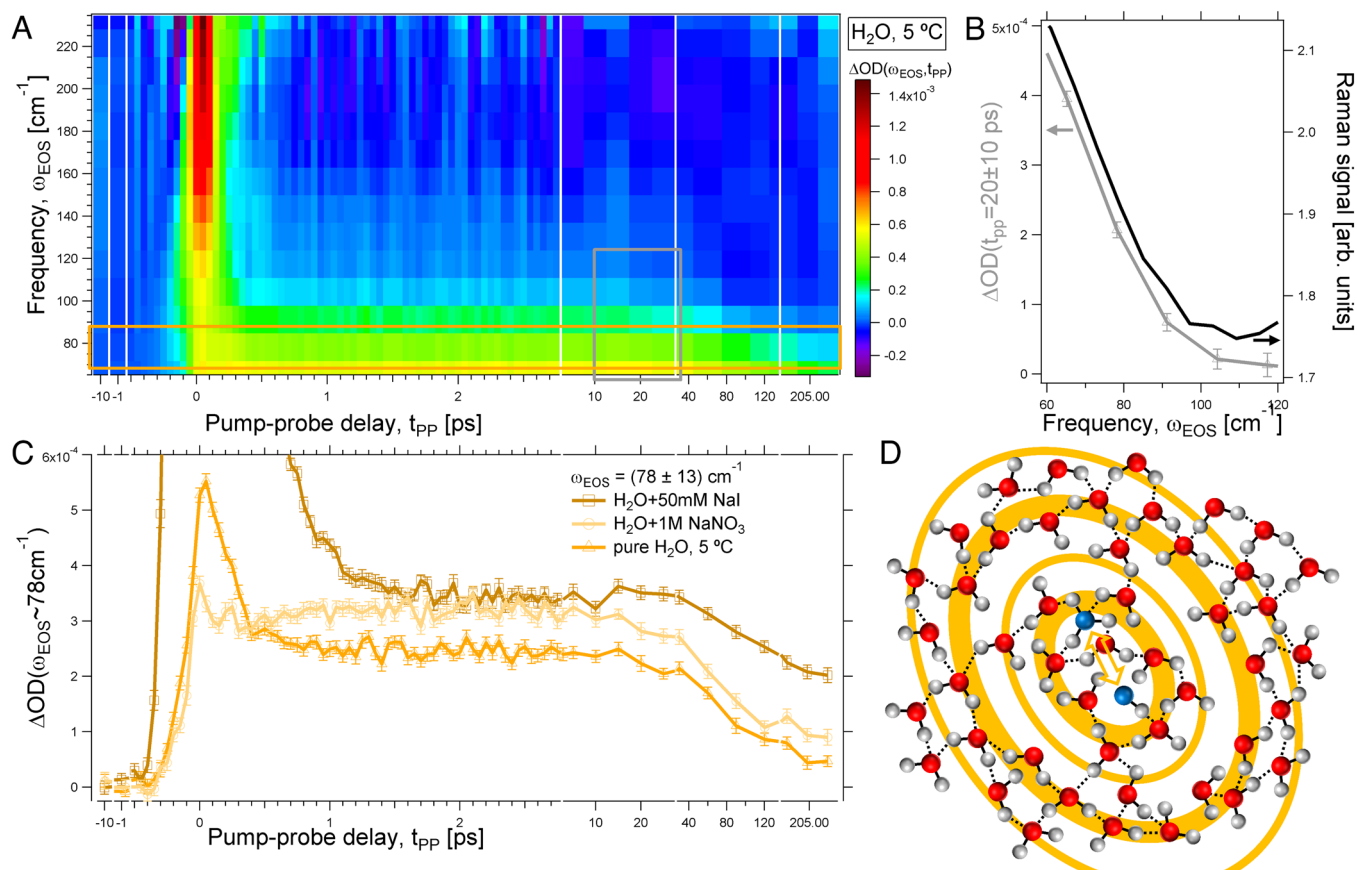

Fig. 3. The photoionization of water triggers collective low-frequency solvent modes. (*A*) Transient change of the optical density, $\Delta OD(\omega_{EOS}, t_{PP})$, as a function of the probed THz frequency (ω_{EOS}) and the pump–probe delay (t_{PP}). (*B*) THz spectrum at $t_{PP} = (20 \pm 10)$ ps, plotted versus probed THz frequency (ω_{EOS}). The gray trace corresponds to an average of ΔOD between $t_{PP} = +10$ ps and $t_{PP} = +30$ ps, as indicated by the gray box in *A*. The black curve is the Raman spectrum of pure water as measured by Walrafen (60). (*C*) THz time-traces at the probe frequency $\omega_{EOS} = (78 \pm 13)$ cm^{-1}, plotted versus pump–probe delay. The traces are obtained by averaging the signal between the THz probe frequency $\omega_{EOS} = 65$ cm^{-1} and $\omega_{EOS} = 91$ cm^{-1}, as indicated by the orange box in *A*. The results on pure water are shown with orange triangles, the results with the scavenger in light orange (circles), and with iodide in dark orange (squares). (*D*) Cartoon of a collective mode launched by the separation of the $OH(H_3O^+)$ complex. The separation between the hydronium cation and the hydroxyl radical (blue oxygen) triggers a solvent perturbation, and a rearrangement of the position of the water molecules (red oxygen). The ripple propagates in the water network.

of hot OH radicals, respectively. Lin et al. (32) performed time-resolved electron diffraction measurements and suggested that the decay of H_2O^+ forms a $OH(H_3O^+)$ complex within 140 fs subsequent to the photoexcitation, followed by the dissociation of $OH(H_3O^+)$ into OH radicals and H_3O^+ after ~250 fs. Thus, a τ_2 between ~130 fs and ~200 fs agrees well with the $50-250$ fs formation time of the relaxed proton in water (32, 62–68) and the lifetime of the transient complex $OH(H_3O^+)$.

Previously, low-frequency intramolecular modes were identified in liquid water with Raman spectroscopy by Walrafen (60). Two broad bands were found, with one centered at $\sim60\,cm^{-1}$ and extending up to $\sim100\,cm^{-1}$. This Raman band overlaps very well with the transient terahertz feature detected here at $\sim60-100\,cm^{-1}$. In ref. 60, the Raman band was assigned to transverse spherical acoustic shear phonons with a wavelength of $\sim8\,Å$ (S-band), corresponding to a rearrangement of the hydrogen-bonded water network involving up to the third nearest neighbors. Most interestingly, Lin et al. (32) reported that, after about 200 fs from the photoionization of a water molecule in the bulk liquid, there is a perturbation of the pair-distribution function—which pinpoints the structural rearrangement of water–up

to about 8 Å. Considering the similar timescale (~200 fs), spectral response ($\sim60-100\,cm^{-1}$), and extent of perturbation of the water structure (~8 Å), we propose that the long-lived terahertz signal detected here is a collective low-frequency intermolecular mode in the solvent triggered by the charge separation of the transient complex $OH(H_3O^+)$ as sketched in Fig. 3D. The observation of bond distance changes beyond the first hydration shell $(5.4-6.2)$ Å in the ultrafast electron diffraction study after 0.5 ps is in line with the rise of the band at 80 cm^{-1} around 200 fs in our OPTP experiment, as these stem from motions within the second solvation shell or even beyond.

Terahertz Fingerprint of the Localized Solvated Electron. We performed AIMD simulations of bulk water in the presence of one electron in a box with 64 waters to follow the localization of the photo-generated electron. In Fig. 4A, we plot the radius of gyration, R_g, of the spin density for one electron (17) in water over a 20 ps trajectory. Initially R_g is large, but converges to an average value of ~2.4 Å within 0.5 ps, in good agreement with previous experiments and theoretical QM/MM calculations (11). We checked whether nuclear quantum effect give rise to major
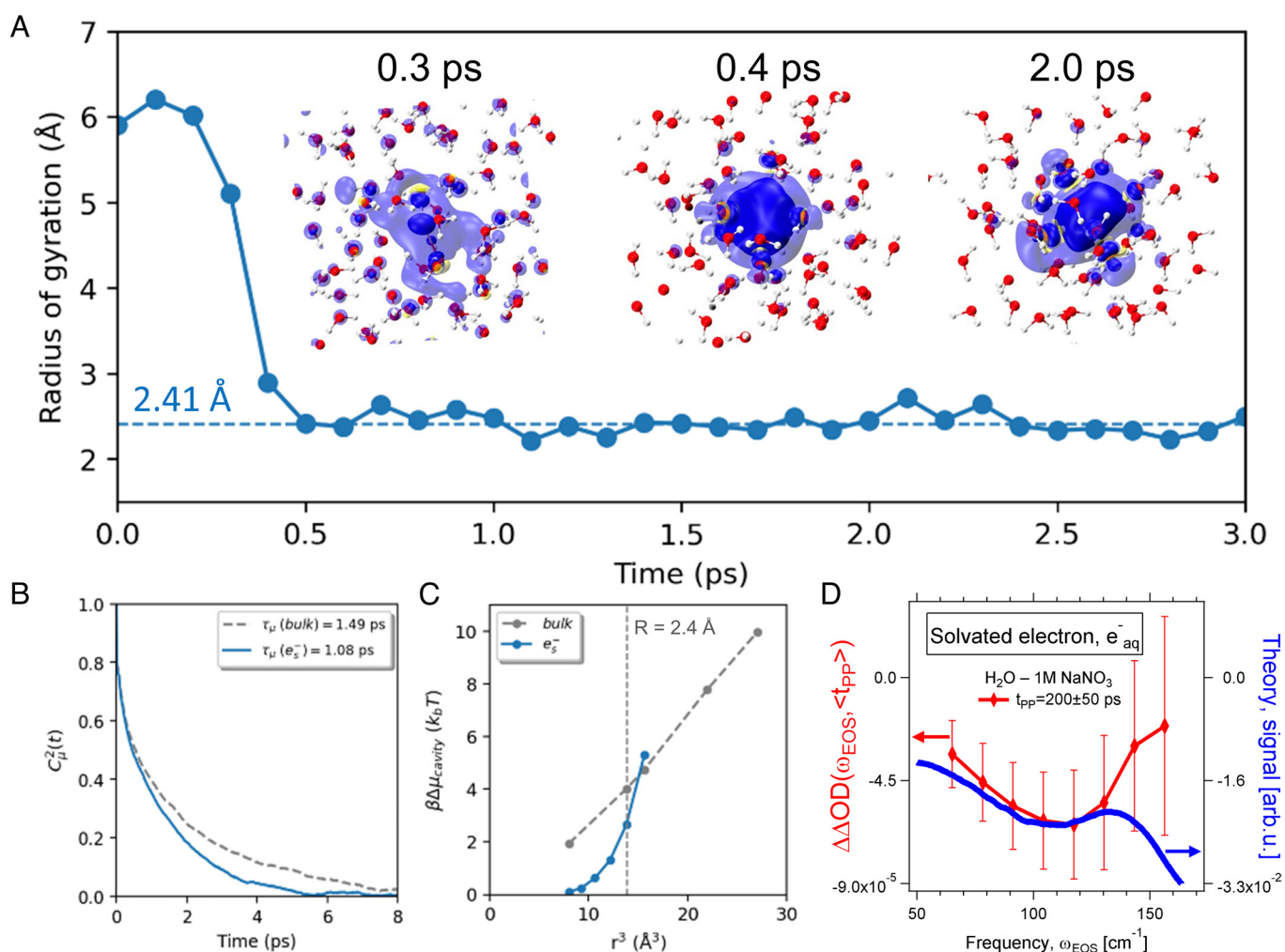

Fig. 4. The solvated electron disrupts the water network. (*A*) The time evolution of gyration radius of electron spin density in neat water with one excess electron. Insets visualize the structures of spin density for some key snapshots. Blue: positive spin density; yellow: negative spin density. Spin density isovalues: opaque: ±0.0015 arb. u.; transparent: ±0.0003 arb. u. (*B*) The theoretical water reorientation lifetime, respectively, for the water molecules in bulk and in the hydration shell of a single excess electron. (*C*) Free energy of cavity formation, μ_{cavity}, for bulk water and the electron cavity. (*D*) With the red curve we plot the difference between the transient optical densities, $\Delta\Delta OD$, experimentally measured in pure water and on a 1 M $NaNO_3$ aqueous solution at 5 °C, at the pump–probe delay $t_{PP} = (200 \pm 50)$ ps, and as a function of THz probe frequency, ω_{EOS}. The transient signal is centered at ~110 cm^{-1}. The results from the simulations are plotted in blue (right axis). See text for details.

changes; however, this was not the case as seen in *SI Appendix,* Fig. S9. In Fig. 4*B*, we examine the hydrogen bond dynamics of the water molecules in the hydration shell of the solvated electron(s). We find that the water reorientation lifetime in the first solvation shell of the electron is significantly smaller compared with bulk water, indicating a weakening of the hydrogen bond network. Further evidence is shown in Fig. 4*C*: At R~2.4 Å, we predict a negligible energy cost needed to create an electron cavity of a given size relative to the free energy cost of cavity formation in the bulk liquid. Furthermore, while the free energy of cavity formation, μ_{cavity}, increases linearly for bulk water, the energy cost of the electron cavity of the solvated electron is highly nonlinear, effectively on par with $k_B T$ but ultimately rapidly exceeding the bulk free energy value at nearly the same value of the cavity size at which the R_g converges to the trapped electron.

While for short pump–probe delays, $t_{PP} = (0 \pm 0.1)$ ps, the difference between the experimental results of the OPTP spectra on pure water and on the aqueous 1 M NaNO$_3$ solution is assigned to the initial spectral response of the delocalized electron (Fig. 2); at longer pump–probe delays, $t_{PP} \gtrsim 1$ ps, we expect that this difference could reveal a signature of the localized, solvated electron. As shown in Fig. 4*C*, experimentally, we find a small, transient, negative THz signal that is centered at ~110 cm^{-1} (red line). This spectral response survives beyond the largest pump–probe delay investigated here, $t_{PP} > 250$ ps. This conforms to the expectations for the spectral signature of a localized solvated electron, since the recombination time of the solvated, relaxed aqueous electrons in water was found to be longer than 300 ps in previous works (8, 11, 12, 23, 24, 42, 43, 61). Thus, we propose that this long-lived signal (~110 cm^{-1}; >250 ps) reveals a spectral feature that is correlated to the long-time response of the aqueous solvated electron that is "trapped" by a solvent cage.

For a direct comparison to the theory, we subtracted the simulated THz spectra of bulk water from the THz spectrum of the localized electron in aqueous solution. In Fig. 4*D*, we compare this with the difference between the experimental photoionization of pure water (with excess electrons) and the scavenged electrons in 1 M NaNO$_3$ (with less electrons). The blue curve in Fig. 4*D* shows that our AIMD calculations reproduce the experimental THz signal (red curve), which is overall negative with a broad minimum at ~110 cm^{-1}, very well. We have to keep in mind that the difference between the photoionization of pure water (with excess electrons) and the scavenged electrons in 1 M NaNO$_3$ (with less electrons), is the difference between a sample with more or less solvated electrons—rather than with and without electrons. Thus, in *SI Appendix,* Fig. S10, we also show ΔOD for the simulated difference of the THz spectra of the two electron aqueous solution from the one aqueous electron, which give also a negative spectral signature, yet with a center frequency which is closer to the bulk water value. Based on the qualitatively good comparison between experiment and theory, the AIMD result allows us to further rationalize the experimental observations and understand the response of the hydration shell of the aqueous solvated electron that is trapped by a solvent cage.

As shown in ref. 11 and in our work, the expected overwhelming contribution to the THz signature, the autocorrelation part of the charge, leaves the THz window within 200 fs. Physically, this spectral contribution describes exclusively those changes that are due to the solvated ion complex, which can be simplified with the particle-box picture. However, when a solute is dissolved in water, the water network rearranges to accommodate it, usually causing an entropic penalty for creation of a cavity, and any changes of the hydrogen bond network is imprinted into the perturbed collective modes in the THz range. Indeed, we have previously found that the water

molecules surrounding alcohols in solution display a specific terahertz band centered at ~165 cm^{-1}, which is red-shifted from the unperturbed water band at ~195 cm^{-1}. The amplitude of the ~165 cm^{-1} hydration water band is correlated to the number of weaker hydrogen bonds (69, 70) of the solute-induced cavity, and is linearly correlated with the changes in entropy (71). For solvated anions and cations, the picture is more complex. Using AIMD simulations, we were able to discern that theoretical THz difference spectra of aqueous salt solutions can be deciphered in terms of only a handful of dipolar autocorrelations and cross-correlations (39), including the self-term of the ion and its cross-correlations with water molecules in the first and second shells, respectively. Physically, the autocorrelations are spectral contributions that exclusively describe changes that are due to the solvated ion complex, in particular its hindered translational motion—or the rattling of the ion in the cage (40). This gives rise to an increase in THz absorption compared with bulk water, with a characteristic anion-specific or cation-specific frequency. In contrast, the cross-correlations quantify the spectral difference due to hydrogen bonding between the first and second solvation shells around the ion in the solution with respect to hydrogen bonds in the pure solvent reference system. While the first—usually overwhelming—contribution is positive in the spectral region between about 50 cm^{-1} and 300 cm^{-1}, the second is negative, centered between 100 cm^{-1} and 200 cm^{-1}, and less ion specific. These are caused by contributions that couple water molecules in the first solvation shell to those in the second shell and give rise to a decrease in absorption compared with bulk water (39, 40).

In the present experiment, we expect also a partial negative cross-correlation describing the spectral difference due to hydrogen bonding between the first and second solvation shells of the electron cavity with respect to standard hydrogen bonds in the pure solvent reference (bulk water), which should be in the frequency range between 100 and 200 cm^{-1} and should be visible during the lifetime of the solvated electron (71). Thus, we expect an overall negative Δα or ΔOD spectral contribution, which should be red-shifted compared with the intermolecular bulk water stretch, in agreement between our AIMD simulations and experimental results in Fig. 4.

Conclusion

In conclusion, our study reveals the dynamical coupling between translational modes in the liquid and photo-generated charge carriers, highlights the spectroscopic fingerprint of hydrated electrons from the solvent perspective, and provides a platform for the examination and investigation of solvated electrons. From OPTP spectroscopy, we can identify a broadband feature, ultra-short lived (<200 fs), and centered at ~180 cm^{-1} corresponding to a particle in a box with a radius of (22 ± 1) Å, i.e., "excitonic" molecular precursors of the solvated electron that are instantaneously generated upon photoexcitation. Upon localization, this autocorrelation THz response will very rapidly blue-shift outside of the THz range. The cross-correlation part is usually less prominent than the autocorrelation part, as it is weaker, of opposite sign and overlaps for monovalent and divalent cations and anions with the overwhelming autocorrelation part. Here, we observe the negative cross-correlation part of the localized electron, which is no longer spectrally overlapping with the positive autocorrelation part after the electron localization, i.e., at $t_{PP} > 0.2$ ps. Due to the sensitivity of our experimental setup, we were able to probe this solvation cavity part without the ion-specific effect, which is a direct probe of the hydrogen bond strength of the cavity and the trace of the birth of a solvated electron in water. As supported by AIMD, we conclude that the hydrogen bond strength is

considerably weakened around the localized electron, which facilitates localization and gives rise to an increase in entropy – in contrast to what was observed before for addition of salts (39, 40) or alcohols (70, 71).

We also discovered a propagating intermolecular Raman mode at $\sim 60 - 100 \, cm^{-1}$, initiated by the solvent rearrangement during charge separation of hydroxyl radicals and hydronium cations, which is found to be only weakly damped with a lifetime of $\sim 150 \, ps$ and centered in the frequency range of the collective hydrogen-bond network motions, extending over several hydration shells (34).

Materials and Methods

Experimental Procedures.

Technique. The experimental setup is detailed in ref. (41). In short, we generated broadband probe pulses in the terahertz range via two-color plasma filamentation in nitrogen. The THz probe pulses were recorded via electrooptical sampling in a 0.1 mm-thick gallium phosphide crystal. The optical pump pulses have a central wavelength of 400 nm, pulse duration of 50 fs, a repetition rate of 0.5 kHz, maximum fluence of $0.28 \, J/cm^2$, and maximum intensity of $\sim 1.4 \, TW/cm^2$. The maximum pump intensity used here is at least ten times smaller than the optical breakdown threshold required to disrupt the jet (72). The instrument response time is estimated in *SI Appendix*, Fig. S2 and amounts to $\tau_R = (90 \pm 9) \, fs$. We took particular care to match the optical-pump and the terahertz-probe spot sizes at the sample position. The laser spots were measured with a camera and amounted to $\sim 400 \, \mu m$ ($1/e^2$) for both the optical pump as well as the terahertz probe beams. For frequencies smaller than about $25 \, cm^{-1}$ (0.75 THz), the terahertz wavelength is larger than the spot size of the optical pump beam (400 μm). Thus, the interpretation of experimental results at frequencies smaller than $25 \, cm^{-1}$ (0.75 THz) is affected by diffraction (73, 74), and we restricted our analysis to frequencies above $25 \, cm^{-1}$, see *SI Appendix*, Fig. S1B. In order to avoid contributions by anisotropy (47, 53), the linear polarizations of the THz-probe and optical-pump beams are set to the magic angle $\sim 54.7°$. A recirculating chiller kept the temperature of the liquid samples to either $5 \pm 0.05 °C$ or $35 \pm 0.05 °C$. The experiments are performed in purged nitrogen atmosphere, with less than 5% humidity. The thickness of the water jets was estimated from the arrival time of the terahertz fields. Monochromatic electromagnetic radiation takes a time $t = d/(c/n) = d \cdot n/c$ to propagate through a medium of thickness d with index of refraction n, with c speed of light. The difference between the time it takes to propagate through two different media with the same thickness is $\Delta t = d \cdot \Delta n/c$, where Δn is the difference between the indexes of refraction. From the black and the blue terahertz field traces transmitted by an equal thickness of air and water, as shown in *SI Appendix*, Fig. S1A, we obtain $\Delta t = 50 \, fs$. If, for simplicity, we assume that the index of refraction of water in the investigated terahertz range is equal to ~ 2 (44–46), we can estimate the thickness of the liquid jet to $d = c \cdot \Delta t/\Delta n \sim 15 \, \mu m$. The jet thickness estimated in this way varied less than 10% in all the experiments reported here.

Data. As displayed in Fig. 1, we estimated the transient variation of the optical density to $\Delta OD\left(\omega_{EOS}, t_{PP}\right) = -\log_{10} \frac{MagFT(E_{ON}(t_{EOS}, t_{PP}))}{MagFT(E_{OFF}(t_{EOS}, t_{PP}))}$, where MagFT is the magnitude of the Fourier transformation, $E_{ON}\left(t_{EOS}, t_{PP}\right)$ is the terahertz field transmitted by the water jet when the pump is ON, $E_{OFF}\left(t_{EOS}, t_{PP}\right)$ is the THz field transmitted by the water jet when the pump if OFF, t_{PP} is the pump–probe delay, t_{EOS} is the electrooptical sampling detection delay, and ω_{EOS} is the frequency. We zero-padded the THz fields to 128 points, and then performed the FT with a Hanning window. The pump-induced change of the phase of the THz fields can be associated with the transient refraction; see *SI Appendix*, Fig. S3. The experimental results reported here and in *SI Appendix* were obtained after averaging 50 independent pump–probe measurements. Each single measurement took approximately 2 h. The error bars indicated in the figures correspond to the standard error of the mean.

Heating. In *SI Appendix*, Fig. S6A, we recorded the optical pump intensity transmitted by the liquid water jet. Due to reflections at the two air–water interfaces of the liquid jet, the transmitted intensity can be estimated as $\frac{n_{H_2O}}{n_{AIR}} \cdot \left(\frac{2n_{AIR}}{n_{AIR}+n_{H_2O}}\right)^2 \cdot \frac{n_{AIR}}{n_{H_2O}} \cdot \left(\frac{2n_{H_2O}}{n_{H_2O}+n_{AIR}}\right)^2 \sim 0.958$, where $n_{AIR} = 1$ and $n_{H_2O} = 1.339$ at 400 nm. This value is plotted with the solid line "reflection

losses" in *SI Appendix*, Fig. S6A. Thus, the amount of energy absorbed by liquid water must be smaller than the error bars of the transmitted pump intensity, which correspond to about 0.5% as shown in *SI Appendix*, Fig. S6A. By considering a jet thickness of 15 μm and a maximum optical pump fluence of $0.28 \, J/cm^2$, we estimate the maximum pump energy density in the liquid sample to be $0.28 \, J/cm^2/(15 \, \mu m) \approx 186 \, J/cm^3$. The maximum amount of energy absorbed by the liquid sample is $0.5\% \cdot 186 \, J/cm^3 \approx 0.93 \, J/cm^3$. This corresponds to a maximum temperature increase of $0.93 \, J/cm^3/(4.2 \, J/cm^3/°C) \approx +0.2 °C$, where $4.2 \, J/cm^3/°C$ is the specific heat of water. Please note that the absorbed energy of multiple laser pulses is not accumulated, because the jet is flowing at a speed that is much faster than the repetition rate of the laser. For details, see ref. 77.

Generation of solvated electrons. Multiple optical-pump optical-probe experiments were previously performed (8, 11, 13, 24, 27, 42, 43) to quantify the amount of solvated aqueous electrons that can be generated in water by three-photon ionization with optical pulses centered at 400 nm. Gobert et al. (43) used a pump intensity similar to the maximum intensity used in the present experiment, $\sim 1.4 \, TW/cm^2$, and measured a concentration of solvated aqueous electrons of 0.38 mM. Similarly, Crowell et al. (42) reported 0.32 mM solvated aqueous electrons. Based on these previous observations, we estimate a concentration of $\sim 0.35 \, mM$ of solvated aqueous electrons generated in our experiments. Correspondingly, within $\sim 200 \, fs$ from the photoexcitation events (32, 62, 76), we expect a presence of $\sim 0.35 \, mM$ hydroxyl radicals (OH) and hydronium cations (H_3O^+) in water.

Nitrate anions (NO_3^-) are well known static and dynamic scavengers (27, 47–50), i.e., they deexcite the molecular water precursors of the solvated aqueous electrons within less than (27, 47, 50) 80 fs (static scavenging), as well as the presolvated and solvated electrons on longer timescales (dynamic scavenging). When compared with bulk water, the number of photo-generated electrons is drastically (>70%) and instantaneously reduced in the presence of sodium nitrate (1 M $NaNO_3$). For a 1 M concentration of NO_3^-, the amount of electrons is reduced by 70% according to ref. 27. According to ref. 50, the amount of electrons is reduced by 88%. No signal of solvated electrons ($\sim 100\%$ reduction) could be found in ref. 47. In summary, the amount of photo-generated electron precursors is decreased by at least 70% in a 1 M solution of sodium nitrate with respect to pure water.

The addition of iodide anions (I^-) in water increases the number of photo-generated electrons. While the iodide anion has no stable excited state in the gas phase, it displays a broad absorption peak around 225 nm when dissolved in water. This broad feature was assigned to charge-transfer-to-solvent (CTTS) bands (51). The resonant excitation of the CTTS band in an iodide aqueous solution with an optical pump pulse close to 225 nm (51–54) results in the generation of a contact pair of a solvated electron and an iodine atom within 300 fs, which later relax and recombine on timescales between ~ 1 and 20 ps. However, the photodetachment mechanism is different when the optical pump pulses are not resonant with the CTTS band (54–56). When the optical pump is set to the central wavelength (55, 56) of 312.5 nm, it was found that the electrons are generated by the three-photon excitation of the iodide anions. When monitored with a delayed optical pulse that probes the population of relaxed solvated aqueous electrons, Long et al. (56) suggested that a "wet electron" is formed from the photo-excited molecular precursor with a time constant of $400 \pm 40 \, fs$, and later it decays into the fully relaxed aqueous electron within $600 \pm 40 \, fs$. These time constants are very similar to the ones reported for bulk water, which were $300 \pm 40 \, fs$ and $540 \pm 40 \, fs$, respectively. By also comparing the recombination times, the authors of ref. 54 indicated that the non-CTTS-resonant ionization of iodide aqueous solutions strongly resembles the photoionization in pure liquid water. In ref. 56, it was shown that the transient signal of the solvated electron from a 1 M solution of sodium iodide is 10× larger than the one in pure water, for a pump excitation intensity of about $0.24 \, TW/cm^2$. Refs. 52 and 54 reported that the amount of photo-generated electrons is roughly proportional to the amount of NaI in solution. In summary, recalling that nonresonant photoionization of an iodide anion requires three photons and that the maximum fluence used in the OPTP experiments reported here is $1.4 \, TW/cm^2$, we expect that the signal associated with the photo-generated electrons in a 50 mM NaI solution should be approximately $\frac{50 \, mM}{1 \, M} \cdot \left(\frac{1.4 \, TW/cm^2}{0.24 \, TW/cm^2}\right)^3 \approx 10$ times larger than the one in

pure water. This would result in about $10 \cdot 0.35 \text{ mM} = 3.5 \text{ mM}$ solvated aqueous electrons and 3.5 mM neutral iodine atoms in the pump-perturbed 50 mM NaI aqueous solution. Please note that in both the nitrate (1 M $NaNO_3$) and iodide (50 mM NaI) solutions we chose sodium as counter ion because it interacts weakly with the photo-generated electrons (77).

Theoretical Procedures.

AIMDs. The AIMDs calculations were performed by CP2K package (78) in a NVT (T = 300 K) ensemble for a system with 64 water molecules in a periodic cubic box with length L = 12.42 Å, which corresponds to the experimental density of bulk water at 300 K (79, 80). The NVT simulation adopts a Nose Hoover thermostat (81) with a time step of 0.5 fs. The system is negatively charged so as to provide excess electron(s). Hybrid functional revPBE0-D3 (79, 80) with Grimme's DFT-D3 dispersion corrections with zero-damping is employed with the Gaussian plane wave (82) pseudopotential method, while Goedecker–Teter–Hutter (83) pseudopotentials with a MOLecularly OPTimised (MOLOPT) basis set at Triple-Zeta for Valence electrons plus Two Polarization functions (TZV2P) level is used with an energy cutoff up to 400 Ry. Each production run achieves a time range up to 20 ps after it reaches equilibrium. The examination of the influence of nuclear quantum effect was performed with the help of i-Pi software (84).

The total dipole moment during the AIMD simulation was calculated using the Wannier functions method and systematically collected to calculate the IR spectroscopy using a linear response method. To be specific, the IR intensity $\alpha(\omega)$ is obatined by the Fouries transform of the autocorrelation function of dipole moment $M(t)$ as denoted by previous literature (34, 79, 80) and shown below, where $F(\omega)$ is a prefactor.

$$\alpha(\omega) = F(\omega) \int_{-\infty}^{\infty} dt e^{i\omega t} < M(0) \cdot M(t) >. \qquad [1]$$

The spread of the spin density of the excess electron was quantitatively evaluated by its gyration radius (17), while the center of the of spin density was collected to calculate the diffusion constant D, according to the Einstein relation as below, where r^2 is the mean squared displacement of the species (15).

$$< r^2 >_{t \to \infty} = 6Dt. \qquad [2]$$

The cavity energy denotes the energy cost that is needed to create a cavity within the system at a certain radius. It can be calculated according to the relation to the probability of finding zero species within the cavity throughout all snapshots, $P_v(0)$. That reads, $P_v(0) = e^{-\beta \Delta \mu_{cav}}$ where $\beta = 1/k_B T$.

The hydrogen-bonded lifetime $C_{HB}(t)$ was calculated as Eq. (**3**), where operator $h(t) = 1$ denotes an intact hydrogen bond and $h(t) = 0$ denotes the disrupted case at time t. The water orientation relaxation lifetime $C_\mu^{(2)}(t)$ is calculated as Eq. (**4**), where P_2 is the second-rank Legendre polynomial and $\mu(t)$ is the dipole moment of studied water at time t.

$$C_{HB}(t) = \frac{< h(0) \cdot h(t) >}{< h(0)^2 >}. \qquad [3]$$

$$C_\mu^{(2)}(t) = \frac{< P_2 [\mu(0) \cdot \mu(t)] >}{< P_2 [\mu(0) \cdot \mu(0)] >}. \qquad [4]$$

Data, Materials, and Software Availability. All study data are included in the article and/or *SI Appendix* in graphic format.

Author affiliations: [a]Department of Physical Chemistry II, Ruhr University Bochum, 44801 Bochum, Germany; [b]Chemical Sciences Division, Lawrence Berkeley National Laboratory, University of California, Berkeley, CA 94720; [c]Kenneth S. Pitzer Center for Theoretical Chemistry, University of California, Berkeley, CA 94720; [d]Department of Chemistry, University of California, Berkeley, CA 94720; [e]Department of Chemical and Biomolecular Engineering, University of California, Berkeley, CA 94720; and [f]Department of Bioengineering, University of California, Berkeley, CA 94720

1. B. C. Garrett *et al.*, Role of water in electron-initiated processes and radical chemistry: Issues and scientific advances. *Chem. Rev.* **105**, 355–389 (2005).
2. K. R. Siefermann, B. Abel, The hydrated electron: A seemingly familiar chemical and biological transient. *Angew. Chemie Int. Ed.* **50**, 5264–5272 (2011).
3. F. Arnold, Solvated electrons in the upper atmosphere. *Nature* **294**, 732–733 (1981).
4. E. Alizadeh, L. Sanche, Precursors of solvated electrons in radiobiological physics and chemistry. *Chem. Rev.* **112**, 5578–5602 (2012).
5. C.-R. Wang, J. Nguyen, Q.-B. Lu, Bond breaks of nucleotides by dissociative electron transfer of nonequilibrium prehydrated electrons: A new molecular mechanism for reductive DNA damage. *J. Am. Chem. Soc.* **131**, 11320–11322 (2009).
6. A. Migus, Y. Gauduel, J. L. Martin, A. Antonetti, Excess electrons in liquid water: First evidence of a prehydrated state with femtosecond lifetime. *Phys. Rev. Lett.* **58**, 1559–1562 (1987).
7. Y. Tan *et al.*, Transient evolution of quasifree electrons of plasma in liquid water revealed by optical-pump terahertz-probe spectroscopy. *Adv. Photonics* **3**, 1–7 (2021).
8. J. L. McGowen, H. M. Ajo, J. Z. Zhang, B. J. Schwartz, Femtosecond studies of hydrated electron recombination following multiphoton ionization at 390 nm. *Chem. Phys. Lett.* **231**, 504–510 (1994).
9. F. H. Long, H. Lu, K. B. Eisenthal, Femtosecond studies of the presolvated electron: An excited state of the solvated electron? *Phys. Rev. Lett.* **64**, 1469–1472 (1990).
10. H. Lu, F. H. Long, K. B. Eisenthal, Femtosecond studies of electrons in liquids. *J. Opt. Soc. Am. B* **7**, 1511 (1990).
11. J. Savolainen, F. Uhlig, S. Ahmed, P. Hamm, P. Jungwirth, Direct observation of the collapse of the delocalized excess electron in water. *Nat. Chem.* **6**, 697–701 (2014).
12. A. Berger, J. Savolainen, A. Shalit, P. Hamm, Note: Deep UV-pump THz-probe spectroscopy of the excess electron in water. *J. Chem. Phys.* **146**, 246101 (2017).
13. P. Kambhampati, D. H. Son, T. W. Kee, P. F. Barbara, Solvation dynamics of the hydrated electron depends on its initial degree of electron delocalization. *J. Phys. Chem. A* **106**, 2374–2378 (2002).
14. P. J. Turi, P. J. Rossky, Theoretical studies of spectroscopy and dynamics of hydrated electrons. *Chem. Rev.* **112**, 5641–5674 (2012).
15. J. M. Herbert, Structure of the aqueous electron. *Phys. Chem. Chem. Phys.* **21**, 20538–20565 (2019).
16. J. M. Herbert, M. P. Coons, The hydrated electron. *Annu. Rev. Phys. Chem.* **68**, 447–472 (2017).
17. J. Wilhelm, J. VandeVondele, V. V. Rybkin, Dynamics of the bulk hydrated electron from many-body wave-function theory. *Angew. Chemie Int. Ed.* **58**, 3890–3893 (2019).
18. J. Lan *et al.*, Simulating the ghost: Quantum dynamics of the solvated electron. *Nat. Commun.* **12**, 1–10 (2021).
19. R. E. Larsen, W. J. Glover, B. J. Schwartz, Does the hydrated electron occupy a cavity? *Science* **329**, 65–69 (2010).
20. L. D. Jacobson, J. M. Herbert, Comment on "Does the Hydrated Electron Occupy a Cavity?" *Science* **331**, 1387–1387 (2011).
21. R. E. Larsen, W. J. Glover, B. J. Schwartz, Response to Comments on "Does the Hydrated Electron Occupy a Cavity?" *Science* **331**, 1387–1387 (2011).
22. L. Turi, Á. Madarász, Comment on "does the hydrated electron occupy a cavity?" *Science* **331**, 2010–2012 (2011).
23. C. G. Elles, A. E. Jailaubekov, R. A. Crowell, S. E. Bradforth, Excitation-energy dependence of the mechanism for two-photon ionization of liquid H_2O and D_2O from 8.3 to 12.4 eV. *J. Chem. Phys.* **125**, 044515 (2006).
24. R. A. Crowell, D. M. Bartels, Multiphoton Ionization of Liquid Water with 3.0-5.0 eV Photons. *J. Phys. Chem.* **100**, 17940–17949 (1996).
25. N. Linz *et al.*, Wavelength dependence of nanosecond infrared laser-induced breakdown in water: Evidence for multiphoton initiation via an intermediate state. *Phys. Rev. B* **91**, 134114 (2015).
26. C. G. Elles, C. A. Rivera, Y. Zhang, P. A. Pieniazek, S. E. Bradforth, Electronic structure of liquid water from polarization-dependent two-photon absorption spectroscopy. *J. Chem. Phys.* **130**, 084501 (2009).
27. T. W. Kee, D. H. Son, P. Kambhampati, P. F. Barbara, A unified electron transfer model for the different precursors and excited states of the hydrated electron. *J. Phys. Chem. A* **105**, 8434–8439 (2001).
28. W. A. Goddard, W. J. Hunt, The rydberg nature and assignments of excited states of the water molecule. *Chem. Phys. Lett.* **24**, 464–471 (1974).
29. P. Gürtler, V. Saile, E. E. Koch, Rydberg series in the absorption spectra of H_2O and D_2O in the vacuum ultraviolet. *Chem. Phys. Lett.* **51**, 386–391 (1977).
30. O. Christiansen, T. M. Nymand, K. V. Mikkelsen, A theoretical study of the electronic spectrum of water. *J. Chem. Phys.* **113**, 8101 (2000).
31. K. Kobayashi, Optical spectra and electronic structure of ice. *J. Phys. Chem.* **87**, 4317–4321 (1983).

32. M.-F. Lin et al., Imaging the short-lived hydroxyl-hydronium pair in ionized liquid water. *Science* **374**, 92–95 (2021).

33. F. Novelli, B. Guchhait, M. Havenith, Towards intense THz spectroscopy on water: Characterization of optical rectification by GaP, OH1, and DSTMS at OPA wavelengths. *Materials (Basel)* **13**, 1311 (2020).

34. M. Heyden et al., Dissecting the THz spectrum of liquid water from first principles via correlations in time and space. *Proc. Natl. Acad. Sci.* **107**, 12068–12073 (2010).

35. M. Cho, G. R. Fleming, S. Saito, I. Ohmine, R. M. Stratt, Instantaneous normal mode analysis of liquid water. *J. Chem. Phys.* **100**, 6672–6683 (1994).

36. G. Cassone, J. Sponer, S. Trusso, F. Saija, Ab initio spectroscopy of water under electric fields. *Phys. Chem. Chem. Phys.* **21**, 21205–21212 (2019).

37. D. C. Elton, M. Fernández-Serra, The hydrogen-bond network of water supports propagating optical phonon-like modes. *Nat. Commun.* **7**, 10193 (2016).

38. F. Novelli, M. Bernal Lopez, G. Schwaab, B. Roldan Cuenya, M. Havenith, Water solvation of charged and neutral gold nanoparticles. *J. Phys. Chem. B* **123**, 6521–6528 (2019).

39. P. Schienbein, G. Schwaab, H. Forbert, M. Havenith, D. Marx, Correlations in the Solute-Solvent Dynamics Reach beyond the First Hydration Shell of Ions. *J. Phys. Chem. Lett.* **8**, 2373–2380 (2017).

40. G. Schwaab, F. Sebastiani, M. Havenith, Ion Hydration and Ion Pairing as Probed by THz Spectroscopy. *Angew. Chemie* **58**, 3000–3013 (2019).

41. C. Hoberg, M. Havenith, Integration of a rapid scanning technique into THz time-domain spectrometers for nonlinear THz spectroscopy measurements. *AIP Adv.* **9**, 035348. (2019).

42. R. A. Crowell et al., Light-induced temperature jump causes power-dependent ultrafast kinetics of electrons generated in multiphoton ionization of liquid water. *J. Phys. Chem. A* **108**, 9105–9114 (2004).

43. F. Gobert et al., Nanosecond kinetics of hydrated electrons upon water photolysis by high intensity femtosecond UV pulses. *Res. Chem. Intermed.* **27**, 901–910 (2001).

44. F. Novelli, J. W. M. Chon, J. A. Davis, Terahertz thermometry of gold nanospheres in water. *Opt. Lett.* **41**, 5801 (2016).

45. P. Lunkenheimer et al., Electromagnetic-radiation absorption by water. *Phys. Rev. E* **96**, 062607 (2017).

46. H. R. Zelsmann, Temperature dependence of the optical constants for liquid H2O and D2O in the far IR region. *J. Mol. Struct.* **350**, 95–114 (1995).

47. C. R. Wang, T. Luo, Q. Bin Lu, On the lifetimes and physical nature of incompletely relaxed electrons in liquid water. *Phys. Chem. Chem. Phys.* **10**, 4463–4470 (2008).

48. Y. Yamamoto, T. Suzuki, Ultrafast dynamics of water radiolysis: Hydrated electron formation, solvation, recombination, and scavenging. *J. Phys. Chem. Lett.* **11**, 5510–5516 (2020).

49. G. P. Horne, S. M. Pimblott, J. A. LaVerne, Inhibition of radiolytic molecular hydrogen formation by quenching of excited state water. *J. Phys. Chem. B* **121**, 5385–5390 (2017).

50. C. D. Jonah, J. R. Miller, M. S. Matheson, The reaction of the precursor of the hydrated electron with electron scavengers. *J. Phys. Chem.* **81**, 1618–1622 (1977).

51. H. Okuyama, Y.-I. Suzuki, S. Karashima, T. Suzuki, Charge-transfer-to-solvent reactions from I-To water, methanol, and ethanol studied by time-resolved photoelectron spectroscopy of liquids. *J. Chem. Phys.* **145**, 074502 (2016).

52. A. Lübcke, F. Buchner, N. Heine, I. V. Hertel, T. Schultz, Time-resolved photoelectron spectroscopy of solvated electrons in aqueous NaI solution. *Phys. Chem. Chem. Phys.* **12**, 14629 (2010).

53. H. Iglev et al., Photoionization dynamics of an aqueous iodide solution: The temperature dependence. *Chem. Phys. Lett.* **403**, 198–204 (2005).

54. J. A. Kloepfer, V. H. Vilchiz, V. A. Lenchenkov, A. C. Germaine, S. E. Bradforth, The ejection distribution of solvated electrons generated by the one-photon photodetachment of aqueous I- and two-photon ionization of the solvent. *J. Chem. Phys.* **113**, 6288–6307 (2000).

55. F. H. Long, H. Lu, X. Shi, K. B. Eisenthal, Femtosecond studies of electron photodetachment from an iodide ion in solution: The trapped electron. *Chem. Phys. Lett.* **169**, 165–171 (1990).

56. F. H. Long, X. Shi, H. Lu, K. B. Eisenthal, Electron photodetachment from halide ions in solution: Excited-state dynamics in the polarization well. *J. Phys. Chem.* **98**, 7252–7255 (1994).

57. P. H. Hahn et al., Optical absorption of water: Coulomb effects versus hydrogen bonding. *Phys. Rev. Lett.* **94**, 037404 (2005).

58. V. Garbuio, M. Cascella, L. Reining, R. Del Sole, O. Pulci, Ab initio calculation of optical spectra of liquids: many-body effects in the electronic excitations of water. *Phys. Rev. Lett.* **97**, 137402 (2006).

59. N. L. Nguyen, H. Ma, M. Govoni, F. Gygi, G. Galli, Finite-field approach to solving the bethe-salpeter equation. *Phys. Rev. Lett.* **122**, 237402 (2019).

60. G. E. Walrafen, Raman spectrum of water: Transverse and longitudinal acoustic modes below ≈300 cm⁻¹ and optic modes above ≈300 cm⁻¹. *J. Phys. Chem.* **94**, 2237–2239 (1990).

61. M. U. Sander, M. S. Gudiksen, K. Luther, J. Troe, Liquid water ionization: Mechanistic implications of the H/D isotope effect in the geminate recombination of hydrated electrons. *Chem. Phys.* **258**, 257–265 (2000).

62. Z.-H. Loh et al., Observation of the fastest chemical processes in the radiolysis of water. *Science* **367**, 179–182 (2020).

63. O. Marsalek et al., Chasing charge localization and chemical reactivity following photoionization in liquid water. *J. Chem. Phys.* **135**, 224510 (2011).

64. M. Thämer, L. De Marco, K. Ramasesha, A. Mandal, A. Tokmakoff, Ultrafast 2D IR spectroscopy of the excess proton in liquid water. *Science* **350**, 78–82 (2015).

65. J. A. Fournier, W. B. Carpenter, N. H. C. Lewis, A. Tokmakoff, Broadband 2D IR spectroscopy reveals dominant asymmetric H5O2+ proton hydration structures in acid solutions. *Nat. Chem.* **10**, 932–937 (2018).

66. F. Dahms, B. P. Fingerhut, E. T. J. Nibbering, E. Pines, T. Elsaesser, Large-amplitude transfer motion of hydrated excess protons mapped by ultrafast 2D IR spectroscopy. *Science* **357**, 491–495 (2017).

67. F. N. Brünig, M. Rammler, E. M. Adams, M. Havenith, R. R. Netz, Spectral signatures of excess-proton waiting and transfer-path dynamics in aqueous hydrochloric acid solutions. *Nat. Commun.* **13**, 4210 (2022).

68. B. J. Siwick, H. J. Bakker, On the role of water in intermolecular proton-transfer reactions. *J. Am. Chem. Soc.* **129**, 13412–13420 (2007).

69. V. Rozsa et al., Wrapping up hydrophobic hydration: Locality matters. *J. Phys. Chem. Lett.* **11**, 4809–4816 (2020).

70. S. Pezzotti et al., Spectroscopic fingerprints of cavity formation and solute insertion as a measure of hydration entropic loss and enthalpic gain. *Angew. Chemie Int. Ed.* **61**, e202203893 (2022).

71. F. Böhm, G. Schwaab, M. Havenith, Mapping hydration water around alcohol chains by THz calorimetry. *Angew. Chemie Int. Ed.* **56**, 9981–9985 (2017).

72. N. Linz, S. Freidank, X.-X. Liang, A. Vogel, Wavelength dependence of femtosecond laser-induced breakdown in water and implications for laser surgery. *Phys. Rev. B* **94**, 1–19 (2016).

73. E. Knoesel, M. Bonn, J. Shan, T. F. Heinz, Charge transport and carrier dynamics in liquids probed by THz time-domain spectroscopy. *Phys. Rev. Lett.* **86**, 340–343 (2001).

74. E. Knoesel, M. Bonn, J. Shan, F. Wang, T. F. Heinz, Conductivity of solvated electrons in hexane investigated with terahertz time-domain spectroscopy. *J. Chem. Phys.* **121**, 394 (2004).

75. F. Novelli, C. Hoberg, E. M. Adams, J. M. Klopf, M. Havenith, Terahertz pump–probe of liquid water at 12.3 THz. *Phys. Chem. Chem. Phys.* **24**, 653–665 (2022).

76. J. Li, Z. Nie, Y. Y. Zheng, S. Dong, Z.-H. Loh, Elementary electron and ion dynamics in ionized liquid water. *J. Phys. Chem. Lett.* **4**, 3698–3703 (2013).

77. B. Abel, U. Buck, A. L. Sobolewski, W. Domcke, On the nature and signatures of the solvated electron in water. *Phys. Chem. Chem. Phys.* **14**, 22–34 (2012).

78. J. Hutter, M. Iannuzzi, F. Schiffmann, J. Vandevondele, Cp2k: Atomistic simulations of condensed matter systems. *Wiley Interdiscip. Rev. Comput. Mol. Sci.* **4**, 15–25 (2014).

79. L. Ruiz Pestana, N. Mardirossian, M. Head-Gordon, T. Head-Gordon, Ab initio molecular dynamics simulations of liquid water using high quality meta-GGA functionals. *Chem. Sci.* **8**, 3554–3565 (2017).

80. L. Ruiz Pestana, O. Marsalek, T. E. Markland, T. Head-Gordon, The quest for accurate liquid water properties from first principles. *J. Phys. Chem. Lett.* **9**, 5009–5016 (2018).

81. S. Nosé, A unified formulation of the constant temperature molecular dynamics methods. *J. Chem. Phys.* **81**, 511–519 (1984).

82. J. Vandevondele et al., Quickstep: Fast and accurate density functional calculations using a mixed Gaussian and plane waves approach. *Comput. Phys. Commun.* **167**, 103–128 (2005).

83. S. Goedecker, M. Teter, J. Hutter, Separable dual-space Gaussian pseudopotentials. *Phys. Rev. B* **54**, 1703–1710 (1996).

84. V. Kapil et al., i-PI 2.0: A universal force engine for advanced molecular simulations. *Comput. Phys. Commun.* **236**, 214–223 (2019).